Phase stabilities of $MgCO_3$ and $MgCO_3$-II studied by Raman spectroscopy, X-ray diffraction and DFT

Jannes Binck,[1,*] Lkhamsuren Bayarjargal,[1] Sergey S. Lobanov,[2] Wolfgang Morgenroth,[1] Rita Luchitskaia,[1] Chris J. Pickard,[3,4] Victor Milman,[5] Keith Refson,[6,7] Dominik B. Jochym,[8] Peter Byrne,[9] and Björn Winkler[1]

[1]*Institut für Geowissenschaften, Goethe-Universität Frankfurt, Altenhöferallee 1, 60438 Frankfurt am Main, Germany*

[2]*Deutsches GeoForschungsZentrum GFZ Telegrafenberg Building D, 14473 Potsdam, Germany*

[3]*Department of Materials Science & Metallurgy, University of Cambridge, 27 Charles Babbage Road, Cambridge CB3 0FS, United Kingdom*

[4]*Advanced Institute for Materials Research, Tohoku University 2-1-1 Katahira, Aoba, Sendai, 980-8577, Japan*

[5]*BIOVIA Dassault Systèmes, 334 Science Park, Cambridge CB4 0WN, United Kingdom*

[6]*Department of Physics, Royal Holloway, University of London Egham, Surrey TW20 0EX, United Kingdom*

[7]*ISIS Facility, Rutherford Appleton Laboratory, Chilton, Didcot, Oxfordshire, OX11 0QX, United Kingdom*

[8]*Scientific Computing Department, Rutherford Appleton Laboratory, Chilton, Didcot, Oxfordshire OX11 0QX, United Kingdom*

[9]*Department of Physics, University of York, Heslington YO10 5DD, United Kingdom*

(Dated: April 3, 2020)

Abstract

Carbonates are the major hosts of carbon on Earth's surface and their fate during subduction needs to be known in order to understand the deep carbon cycle. Magnesite ($MgCO_3$) is thought to be an important phase participating in deep Earth processes, but its phase stability is still a matter of debate for the conditions prevalent in the lowest part of the mantle and at the core mantle boundary. Here, we have studied the phase relations and stabilities of $MgCO_3$, at these P,T-conditions using Raman spectroscopy at high pressures ($\sim$148 GPa) and after heating to high temperatures ($\sim$3600 K) in laser-heated diamond anvil cell experiments (LH-DAC). The experimental Raman experiments were supplemented by X-ray powder diffraction data, obtained at a pressure of 110 GPa. Density functional theory-based model calculations were used to compute Raman spectra for several $MgCO_3$ high pressure polymorphs, thus allowing an unambiguous assignment of Raman modes. By combining the experimental observations with the DFT-results, we constrain the phase stability field of $MgCO_3$ (magnesite) with respect to the high pressure polymorph, $MgCO_3$-II. We further confirm that Fe-free $MgCO_3$-II is a tetracarbonate with monoclinic symmetry (space group $C2/m$), which is stable over the entire P,T-range of the Earth's lowermost mantle geotherm.

I. INTRODUCTION

The Earth's mantle is believed to experience a carbon influx on the order of teragrams per year, due to the subduction of oceanic lithosphere [1, 2]. Carbonate minerals are considered to constitute the major carbon source during subduction processes [2–6]. In the mantle, decomposition reactions of carbonates and reactions with silicates are thought to lead to the formation of other carbon containing phases [7–10]. As silicates can only incorporate very minor amounts of carbon at mantle conditions [11, 12], the most prevalent carbon bearing phases are believed to be diamond [13], high P,T phases of CO_2 [14], or metal carbides [15, 16]. However, carbonates may survive in the Earth's mantle in cold oxidized subducting slabs [17, 18] some of which might penetrate into the lowermost mantle [19]. This model is supported by the presence of carbonate inclusions ($CaCO_3$, $MgCO_3$, $CaMg(CO_3)_2$) in mantle xenoliths and in super deep diamonds [20–25].

Magnesite ($MgCO_3$) is thought to be stable under P,T-conditions of the Earth's mantle [9, 26, 27]. While other carbonates undergo several phase transitions (e.g. calcite ($CaCO_3$)) [28], or decompose at P,T-conditions of the Earth's mantle (e.g. dolomite ($CaMg(CO_3)_2$) and siderite

* binck@kristall.uni-frankfurt.de

($FeCO_3$)) [29, 30], magnesite remains stable up to at least 80 GPa and 3000 K [26, 31, 32]. Studies of reactions of $MgCO_3$ with SiO_2 implied that high pressure, high temperature polymorphs of $MgCO_3$ might coexist with silicates in super cold slabs in the lower mantle [9]. Model calculations of reactions of $MgCO_3$/$CaCO_3$ with MgO/$MgSiO_3$ under P, T-conditions of the Earth's lower mantle imply the possible existence of oxidized carbon in the form of $MgCO_3$ in the absence of iron [33, 34].

Based on in-situ powder X-ray diffraction, Isshiki *et al.* [26] showed that magnesite ($R\bar{3}c$, Z = 6) undergoes a phase transition to 'magnesite-II' at deep lower mantle conditions ($>$115 GPa and 2200 K). Shortly after these findings, DFT-based predictions reported the possibility of the existence of very high pressure (e.g., at pressures $>$80 GPa) carbonate structures that are characterized by sp^3-hybridized bonding environments within CO_4^{4-} tetrahedrons instead of triangular sp^2-hybridized CO_3^{3-} groups [35–39]. Within the last decade, the existence of so-called 'tetracarbonates' has been confirmed by several experimental studies [30, 40–45].

Several theoretical structures have been reported for sp^3-$MgCO_3$ polymorphs [35, 38, 39]. Combined results from DFT and X-ray powder diffraction suggested a $MgCO_3$ structure with space group $C2/m$ and Z = 12 formula units to be the most stable phase at pressures between 82 – 138.1 GPa [38]. However, a comparison of powder X-ray diffraction data of the $C2/m$-phase with powder patterns published by Isshiki *et al.* [26] gave an unsatisfactory match. Further experimental evidence for the formation of the $C2/m$-phase around $\sim$82 GPa was given by Boulard *et al.* [40] and Maeda *et al.* [9]. However, their data analyses relied on Le Bail fits only. While X-ray powder diffraction data were fitted with the $C2/m$-phase between 85–152 GPa in the study by Maeda *et al.* [9], a lower symmetric structure with space group $P2_1/c$ was proposed to be better suited for fitting X-ray diffraction patterns by Boulard *et al.* [40] at 82 GPa.

Using a sample with an initial composition of $Fe_{0.15}Mg_{0.85}CO_3$ at ambient conditions, Chariton *et al.* [46] have been able to solve the crystal structure of $Fe_{0.4}Mg_{2.6}C_3O_9$ at 98 GPa and after heating to 2500 K from single-crystal data. This structure was shown to be identical to the $C2/m$-phase proposed by Oganov *et al.* [38].

While the existence of the $C2/m$-phase seems now to be established for pressures $<$100 GPa and temperatures $<$2500 K [46], significant gaps and inconsistencies remain in our understanding of the high P, T behaviour of Fe-free $MgCO_3$ [9, 26, 38, 39]. Currently, all experimental data above 100 GPa rely on poorly constrained indexing of X-ray powder diffraction patterns [9, 26, 38], while theoretical calculations suggest several possible low energy structures [35, 38, 39]. The

strength of vibrational spectroscopy for the detection of high pressure, high temperature phases in the diamond anvil cell has recently been exploited for high pressure studies on different carbonates [28, 29, 42, 45, 47–49]. Raman spectroscopy is a very sensitive method, which may provide additional structural information for the particular high pressure, high temperature polymorphs of $MgCO_3$ thus complementing previous X-ray diffraction studies. However, studies that have been employing Raman spectroscopy on $MgCO_3$ are limited to pressures $<$55 GPa [32, 47, 50, 51].

In this study, we have investigated the $MgCO_3$-system in the entire pressure and temperature range reaching to the uppermost part of the Earth's outer core corresponding to pressures up to $\sim$148 GPa and temperatures up to $\sim$3600 K. We combined Raman spectroscopy in the laser heated diamond anvil cell with DFT-based model calculations. Supplementary X-ray powder diffraction data were obtained at high pressures, which support our observations further.

II. METHODS

Syntheses, preparations of experiments, sample characterizations at ambient conditions, as well as Raman spectroscopy in the LH-DAC have been carried out at the Institute of Geosciences at the Goethe Universität Frankfurt, Germany. The high pressure X-ray diffraction experiments have been carried out at P02.2 at PETRA III (DESY) in Hamburg, Germany.

A. Synthesis

Single crystals of magnesite were synthesized according to the method described by Ni *et al.* [52]. All chemicals (magnesium acetate tetrahydrate, hexamethylenetetramine and sodium sulfate) were analytical grade reagents purchased from Merck KGaA (Darmstadt) and used as received without further purification. 3 mmol magnesium acetate, 3 mmol hexamethylenetetramine, and 0.6 g sodium sulfate were dissolved in 40 ml bidistilled water. After stirring for 30 min, the obtained transparent solution was transferred into a 60 ml Teflon cup, which was filled to 60 % of its volume. Subsequently, the cup was put into a stainless steel autoclave and sealed tightly. After reaction at 160° for 48 h, the autoclave was slowly cooled down (160 – 100 °C in 48 h, then 100 – 25 °C in 12 h). The precipitate was filtered under vacuum, washed with distilled water repeatedly and dried at 60 °C in an oven. The slow cooling allowed us to grow crystals with edge lengths up to 60 µm.

B. Characterization

The phase purity of the synthesized batch of single crystals has been characterized at ambient conditions by X-ray powder diffraction. Therefore, we separated the majority of single crystals from the synthesized batch and grounded a fine sample powder in an agate mortar. The grounded sample powder was measured using an X'Pert Pro diffractometer equipped with a linear position-sensitive detector from PANanytical (PIXcel^{3D}) and a Johannson monochromator (Ge 111) using Cu$K\alpha_1$ radiation (λ = 1.5418 Å) generated at 40 kV and 30 mA. A Rietveld refinement was carried out using the GSAS-II software [53] and a reported structure of magnesite [54] as a starting model (see appendix Fig. 1 and Tab. 1-2). The refined lattice parameters were $a = b$ = 4.6375(1) Å, c = 15.0268(2) Å and V = 279.876(1) Å^3, which are consistent with the parameters of the established structure of magnesite [54]. Additionally, Raman spectroscopy was carried out at ambient conditions on single crystals. The spectra confirmed the excellent sample quality (Fig. 1).

C. Preparation of high-pressure, high-temperature experiments

High-pressure, high-temperature experiments were carried out using Boehler-Almax diamond anvil cells (DAC) [55]. Type Ia and IIas diamonds with low birefringence and ultra low fluorescence having either regular culets (200, 250 and 350 µm diameter), or beveled culets (9° bevel, 100 µm inner- and 220 µm outer diameter) were inserted in WC seats. The opening angles of the cells were 48° or 70°. Depending on the culet size, sample chambers of 45 – 160 µm in diameter were laser drilled in Re gaskets pre-indented to ∼40 µm. Before loading, the sample material was dried at 150 °C for 24 h in an oven. Immediately after drying, three diamond anvil cells were loaded with single crystals and one cell with a compacted powder. The single crystals had edge lenghts of ∼15 µm. All cells were loaded with a ruby pressure marker. Neon served as a pressure transmitting medium for the single crystal cells, which was loaded by a custom built gas loading system. In order to obtain X-ray powder diffraction data without any interference by the pressure transmitting medium, no Neon gas was used for the DAC loaded with the compacted powder sample. No further thermal insulation was added to the loadings, in order to prevent possible chemical reactions.

D. Raman spectroscopy in the LH-DAC

Raman spectra were measured in 0.5 – 4 GPa steps upon compression and decompression covering a range between ambient pressure and ∼148 GPa. A frequency doubled 532.14 nm Nd:YAG Oxxius laser (LCX-532S) was focused on the sample with a spot size of 6 µm. Spectra were collected in backscattering geometry, using a grating spectrometer (Acton, SP-2356) equipped with a CCD detector (Pixis 256E) and a microscope objective (Mitutoyo). The spectral resolution of the spectrometer is 3 cm^{-1} [28]. The laser power was set to 430 mW and spectra were collected for 50 s in a frequency window of 100 – 1500 cm^{-1}, using a grating of 1800 grooves/mm. The estimated laser power on the sample was around ∼350 mW. For measurements up to 95 GPa, the pressure was determined before and after the Raman measurement, using the ruby reference scales for non- [56] and quasi-hydrostatic conditions [57]. Pressures were further determined for $P \geq 45$ GPa using the diamond edge reference scale [58]. For $P > 95$ GPa only the diamond edge reference scale was employed. According to Dewaele *et al.* [59], the uncertainty in pressures determined by Mao *et al.* [56] increases from 0.05 GPa at 1 GPa up to 2 GPa at 150 GPa. The accuracy of our pressure determination by the ruby and diamond reference scales was $\leq$2 GPa, while pressure gradients may have caused uncertainties up to 4 GPa during and after laser heating.

The sample was heated from both sides with a pulsed CO_2 laser (Diamond K-250 from Coherent, λ = 10.6 µm) [28]. For the spectroradiometric temperature determination we used the same set-up as for the Raman measurements, while the grating was set to 150 grooves/mm. In order to achieve coupling of the CO_2 heating laser from both sides of the sample, the laser power was typically set in a range between 1 – 6 W, depending on the pressure and the loading of the diamond anvil cell. The heating laser was focused on the sample so that the diameter of the heated area was around 25 µm, which nearly covered all of the single crystals. However, due to the poor to moderate coupling of the laser with the samples, heating was inhomogeneous. Hence, we moved the heating laser across the sample, while typically heating for about 5 min per position. The position of the Raman laser with respect to the heated areas on the sample was controlled using an optical camera. The thermal emission of the sample, as well as the Raman signal was measured with a spatial resolution of around 5 – 6 µm, i.e. the areas for the measurements were significantly smaller than the heating spots. The temperatures during laser heating were determined by the two-colour pyrometer method, employing Planck and Wien fits [60]. We assume a typical uncertainty associated with radiometric temperature measurements in LH-DACs of ∼10 %.

E. High-pressure X-ray diffraction

High pressure X-ray powder diffraction measurements have been carried out at the extreme conditions beamline P02.2 at PETRA III (Desy, Hamburg, Germany). X-ray diffraction data were collected for a $MgCO_3$ powder sample, which at first was pressurized to 110 GPa in a diamond anvil cell and temperature quenched after laser-heating to $\sim$2500 K. The diffraction patterns were acquired using a wavelength of 0.2898 Å, a beam focused to 8×3 µm^2 (full width at half maximum), compound reflective lenses, and a Perkin Elmer XRD 1621 flat-panel detector. A grid of 5×5 points with spacings of 2 µm between each point was measured. The DAC was rotated by $\pm 10^\circ$ with an exposure time of 40 s for every data point collection. The sample-to-detector distance of 402.78 mm and the wavelength were determined employing a CeO_2 reference sample. The diffraction data were processed with the Dioptas software [61]. Rietveld refinements were carried out using the GSAS-II software [53] and the structure model based on an earlier description of the $C2/m$-phase [38].

F. Density functional theory

In order to obtain theoretical Raman spectra, density functional perturbation theory (DFPT) calculations were performed employing the CASTEP code [62]. The code is an implementation of Kohn–Sham DFT based on a plane wave basis set in conjunction with pseudopotentials. The plane wave basis set allows to achieve numerically converged results in a straightforward manner, as the convergence is controlled by a single adjustable parameter, the plane wave cut-off, which we set to 1020 eV. For calculations for pressures $<$100 GPa, the norm-conserving pseudopotentials were generated 'on the fly' from the information provided in the CASTEP data base. These pseudopotentials have been tested extensively for accuracy and transferability [63]. For calculations at pressures $>$100 GPa norm-conserving pseudopotentials with smaller core radii were constructed, in order to avoid overlap of ionic cores. The descriptors of these pseudopotentials are given in the appendix. All calculations employed the GGA-PBE exchange-correlation functional [64]. The Brillouin zone integrals were performed using Monkhorst–Pack grids [65] with spacings between grid points of less than 0.037 Å^{-1}. Geometry optimizations were defined as being converged when the energy change between iterations was $<0.5\times10^{-6}$ eV/atom, the maximal residual force was $<$ 0.01 eV/Å, and the maximal residual stress was $<$ 0.02 GPa. Phonon frequencies were ob-

tained from density functional perturbation theory (DFPT) calculations. Raman intensities were computed using DFPT in the '$2n + 1$' theorem approach [66].

III. RESULTS AND DISCUSSION

A. $MgCO_3$ (magnesite) at high-pressures and high temperatures measured by Raman spectroscopy

The characteristic Raman phonon frequencies of $MgCO_3$ (magnesite) were measured in four different experimental runs, covering a pressure range between ambient pressure and $\sim$107 GPa (Fig. 1 and 2). According to group theory, the following Raman and infrared active modes are expected for magnesite at ambient conditions: $\Gamma = \mathrm{A_{1g}(R)} + 3\mathrm{A_{2u}(IR)} + 5\mathrm{E_u(IR)} + 4\mathrm{E_g(R)}$. All Raman active modes were observed at ambient conditions. Starting at ambient pressure with a frequency of 1444 cm^{-1}, the $\mathrm{E_g}(\nu_3)$ mode is obscured by the first order Raman mode of the diamond anvils in the DAC experiments. The frequencies of the symmetric stretching mode and the symmetric in-plane bend allow a straightforward identification of the CO_3^{2-}-groups [50, 67, 68]. We observed the $\mathrm{A_{1g}}(\nu_1)$ and $\mathrm{E_g}(\nu_4)$ modes up to $\sim$107 GPa in a range between 1095 – 1304 cm^{-1} and 740 – 893 cm^{-1} respectively. The two low frequency $\mathrm{E_g}$ modes (ν = 213 and 331 cm^{-1} at ambient pressure) were observed up to 45.5 GPa. At higher pressures these modes displayed a significant broadening, or disappeared completely. A similar behaviour for the low frequency $\mathrm{E_g}$ modes was reported by Williams *et al.* [50] and Gillet [51], who observed the 213 cm^{-1} Raman band at pressures between 13 – 20 GPa and the 331 cm^{-1} Raman band up to 26 GPa.

We were able to detect all Raman active modes that are observable in a diamond anvil cell up to 87.8 GPa by carefully thermally annealing the single crystal at nearly each pressure step up to 82 GPa and measuring the Raman signal after temperature quenching (Fig. 1). The temperatures during the thermal annealing by the laser were estimated to be $<$1000 K, since no visible thermal radiation was observed. An offset for especially the low frequency Raman modes may be observed for some of the high pressure Raman spectra due to the non-hydrostatic pressure on the sample. These effects disappeared after heating was applied and hydrostatic conditions on the sample were increased.

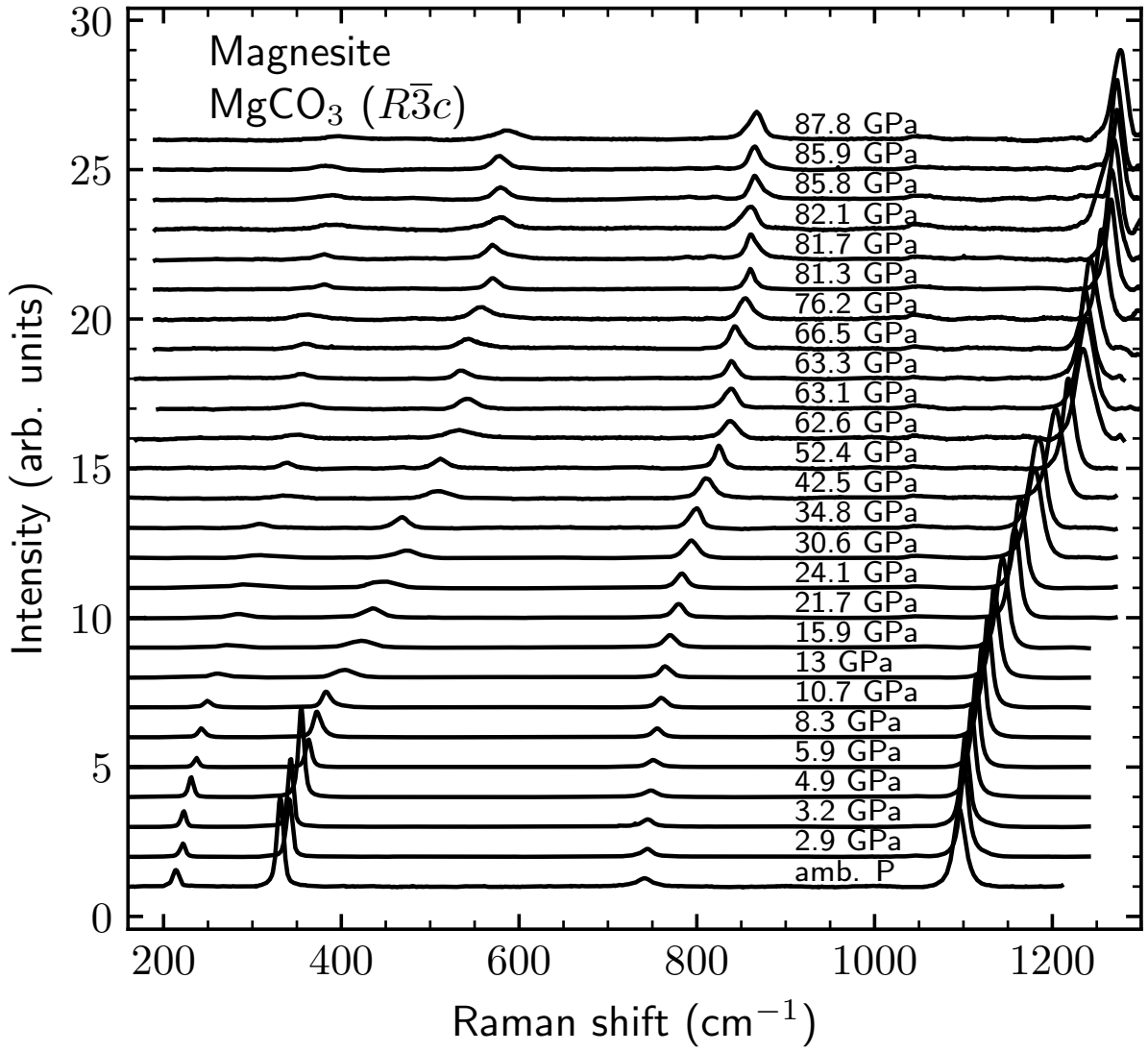

FIG. 1. High pressure Raman spectra of $MgCO_3$ (magnesite) from ambient pressure to $\sim$88 GPa as obtained for a single run. For most of the pressure steps between 15.9 and 82.1 GPa, the crystal was slightly annealed at temperatures $<$1000 K. All Raman measurements were conducted after quenching the sample to ambient temperature.

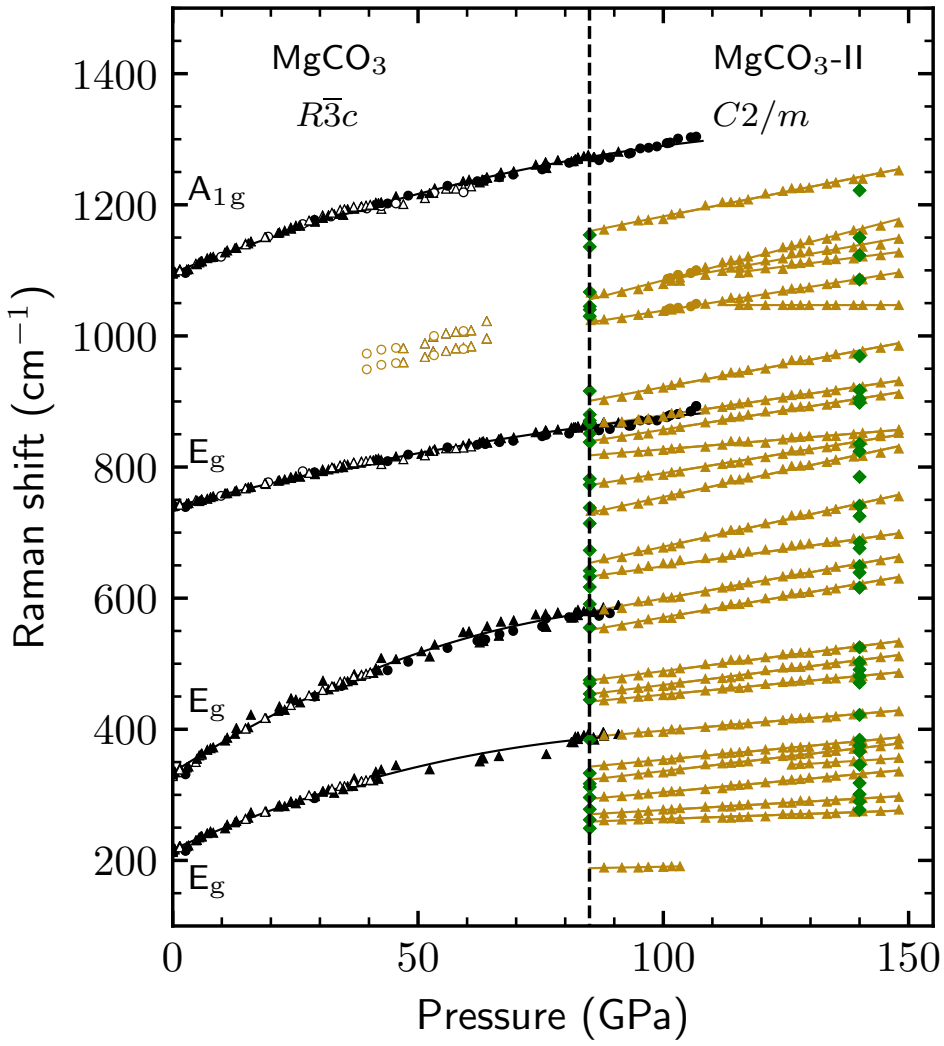

FIG. 2. Pressure dependence of the characteristic Raman modes of magnesite (black symbols) and $MgCO_3$-II (yellow symbols). Triangles and circles correspond to single crystal and powder samples respectively. Open symbols correspond to data obtained under cold-decompression. DFT-calculated phonon frequencies of $MgCO_3$-II at 85 and 140 GPa are shown for comparison (green diamond symbols). The black dashed line marks the phase boundary of the $MgCO_3$ polymorphs at 85 GPa. Data points were fitted using linear or quadratic fits. (color online)

B. Phase transition of $MgCO_3$ (magnesite) to $MgCO_3$-II identified by Raman spectroscopy, XRD and density functional theory

At 83 GPa and after heating to ∼2400 K, our Raman spectra still indicate the presence of $MgCO_3$ (magnesite) at these conditions, while a drastic change in the spectra is observed at around 85 GPa and after heating to ∼2000 K, where new characteristic Raman bands were observed besides those of $MgCO_3$ (magnesite) (appendix Fig. 2). At 87.9 GPa and after heating to maximum temperatures of ∼3100 K, Raman spectra yielded at least 23 strong intense modes covering a frequency range between 250 and 1250 cm^{-1} (Fig. 3). These changes are due to a phase transition from $MgCO_3$ (magnesite) to a second phase, which we have labeled $MgCO_3$-II here. We computed the Raman spectra for the monoclinic $C2/m$-phase [38, 46] and for a hypothetical triclinic $P\bar{1}$-phase [39], which has been suggested to be stable between 85 – 101 GPa. The experimental Raman spectrum at 87.9 GPa can very satisfactorily be explained by a combination of the theoretical Raman spectra of magnesite and the $C2/m$-phase, while no indication for the $P\bar{1}$-phase was found (Fig. 3).

We continued measuring Raman spectra up to 148 GPa (Fig. 2 and 4). For most of the pressure steps, the sample was heated up to maximum temperatures of ∼3600 K prior to the measurement, in order to achieve a hydrostatic pressure distribution on the sample. A comparison of theoretical spectra with experimental data at 115 and 140 GPa shows an excellent match of frequencies and intensities (Fig. 5). Characteristic modes of $MgCO_3$ (magnesite) are no longer observed in the experimental spectrum at these conditions. According to group theory, the irreducible representations of the $C2/m$-phase for the Raman and infrared-modes are $\Gamma = 25\mathrm{A_g(R)} + 18\mathrm{A_u(IR)} + 20\mathrm{B_g(R)} + 24\mathrm{B_u(IR)}$. The tetrahedral CO_4^{4-} groups of the $C2/m$-phase are polymerized and form corner sharing $C_3O_9^{6-}$ rings [38]. Between 85 and 148 GPa, characteristic vibrations of those rings are frequencies in the ranges 1023 – 1095 cm^{-1}, 1026 – 1128 cm^{-1}, 1050 – 1146 cm^{-1}, and 1065 – 1173 cm^{-1}, respectively. Further characteristic features are the intense A_g and B_g modes at 733 – 781 cm^{-1} and 444 – 463 cm^{-1}, respectively. Both modes are due to relative movements between the $C_3O_9^{6-}$ rings and the Mg^{2+} cations. Two modes in $MgCO_3$-II at 189 cm^{-1} ($\leq$105 GPa) and 1050 cm^{-1} ($\geq$120 GPa) have no correspondence in the DFT-calculations. The origin of these modes is currently unexplained.

There have been suggestions that the $C2/m$ polymorph transforms into another phase at $P \geq$138 GPa. For this phase, structures with space group $P2_1$ [38], or $P2_12_12_1$ [39] have been

suggested. Theoretical Raman spectra of the hypothetical $P2_1$-phase [38] at 120 and at 140 GPa were computed and compared to our experimental observations (see appendix Fig. 3). Although the comparison between experimental and theoretical spectra exhibits some similarities at higher frequencies, significant differences are observed in the lower frequency range. Hence, we conclude that this phase has not been formed in our experiments. Computation of the Raman spectra of the $P2_12_12_1$-phase [39] was beyond the available computation resources.

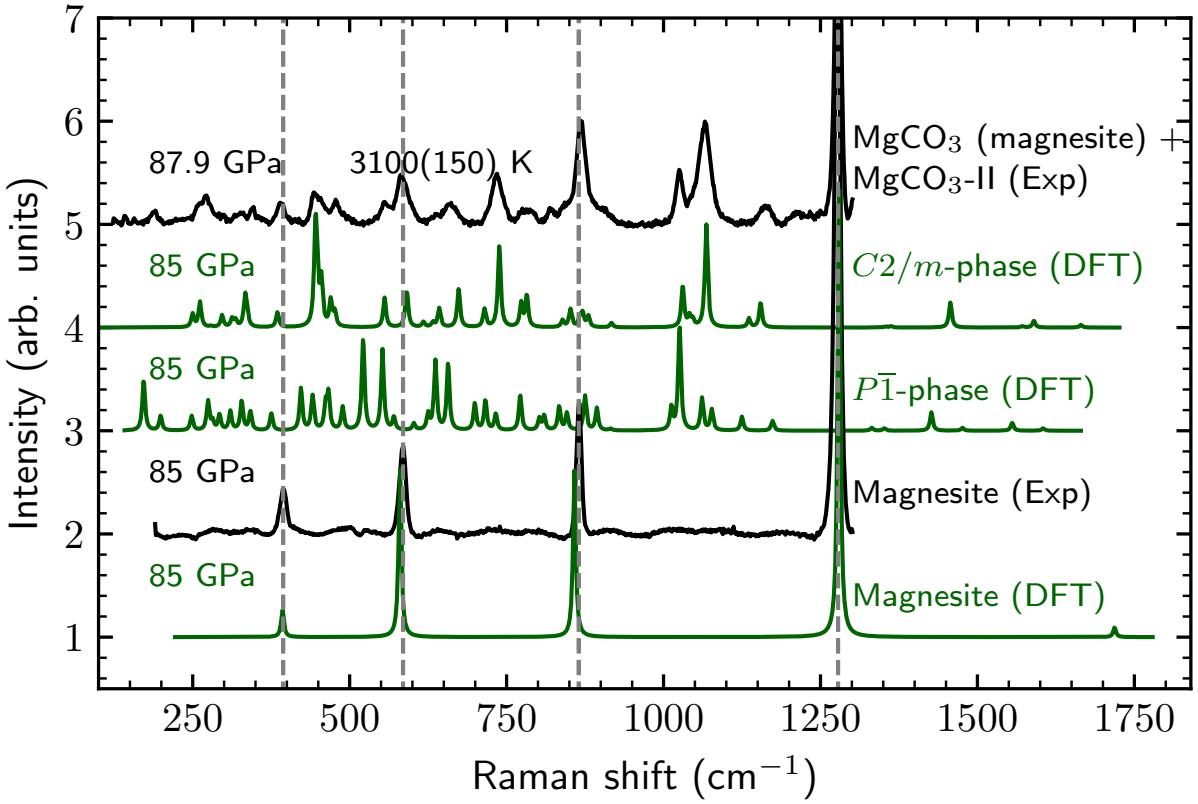

FIG. 3. Experimental Raman spectra of $MgCO_3$ (magnesite) and a mixture of $MgCO_3$ (magnesite) and $MgCO_3$-II ($C2/m$-phase [38]) are shown in black. DFT-calculated Raman spectra of magnesite, the $C2/m$-phase and the $P\bar{1}$-phase [39] are shown in green. DFT frequencies were calculated with a FWHM broadening of 5 cm^{-1}. The calculated frequencies were multiplied by a scaling factor of 1.02. The characteristic Raman modes of $MgCO_3$ (magnesite) at 85 GPa are indicated by dashed grey lines. (color online)

Our combined results from Raman spectroscopy and DFT-calculations are supported by synchrotron X-ray powder diffraction measurements, which have been conducted on $MgCO_3$ powder at 110 GPa and after heating to ~2500 K. We were able to successfully carry out a Rietveld refinement, which allowed the identification of the $C2/m$-phase (Fig. 6 and appendix Tab. 1-2). Since

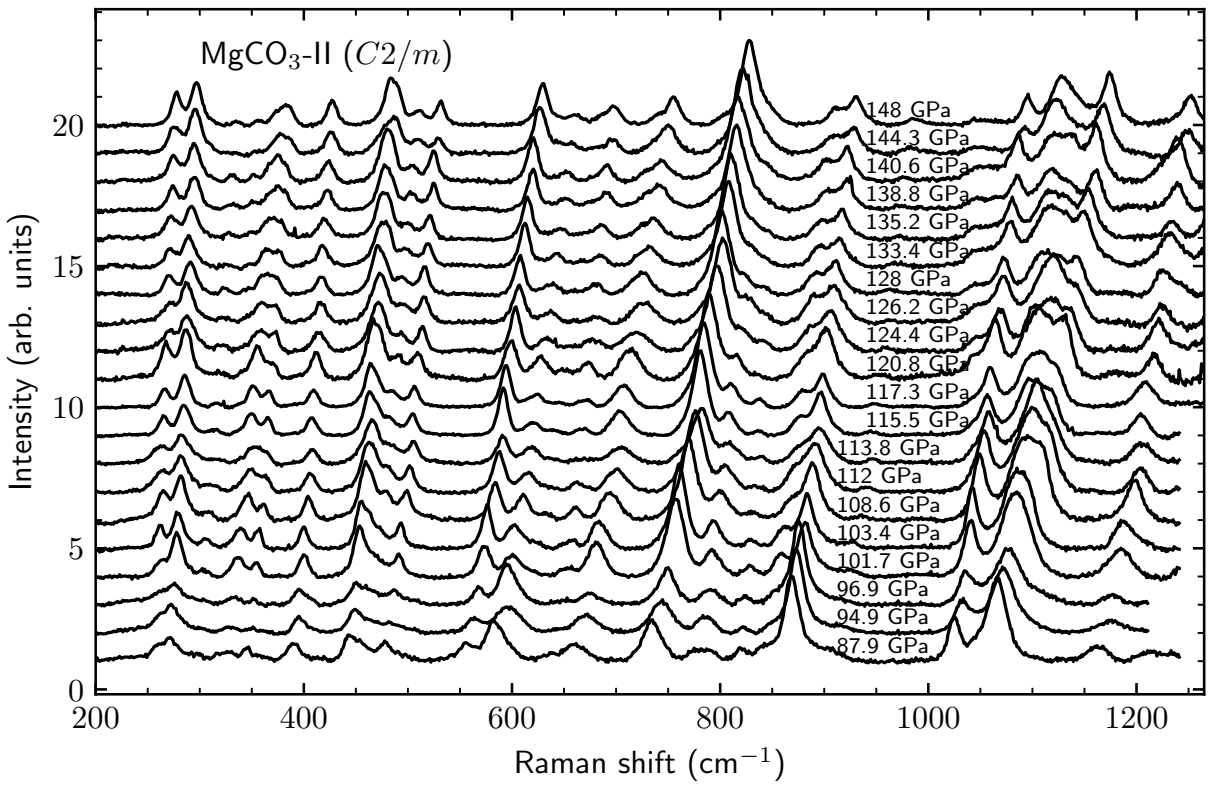

FIG. 4. Raman spectra of $MgCO_3$-II ($C2/m$-phase) [38] in a pressure range from 87 to 148 GPa for a single run. For most of the pressure steps, the sample was heated to maximum temperatures between 3000 and 3600 K and measured after quenching to ambient temperature. For the present data, the grating of the Raman spectrometer was centered towards higher Raman shifts, which resulted in obscuration of the CO_3-stretching mode (ν = 1278 cm^{-1}) by the diamond anvils.

Rietveld refinements are usually hard to conduct for high pressure data especially after heating, intensities of a grid of 25 diffraction images were summed at each particular 2 theta angle, in order to achieve an accurate ratio of intensities for the refinement (appendix Fig. 4-5). Profile parameters including scaling, Gaussian and Lorentzian terms, as well as the unit cell were initially refined. The background was manually fitted, using a Chebychev function with twenty terms. In order to reduce the number of parameters, we constrained the isotropic atomic displacement parameters to be the same for symmetrically independent atoms of the same chemical species. Further, we employed restraints on the atomic distances and refined the atomic positions. Refined lattice parameters were a = 8.117(4) Å, b = 6.510(1) Å, c = 6.911(2) Å, β = 103.858(9)°, V = 354.64(5) $Å^3$. Our refined structural model is in excellent agreement with the structure of the $C2/m$-phase re-

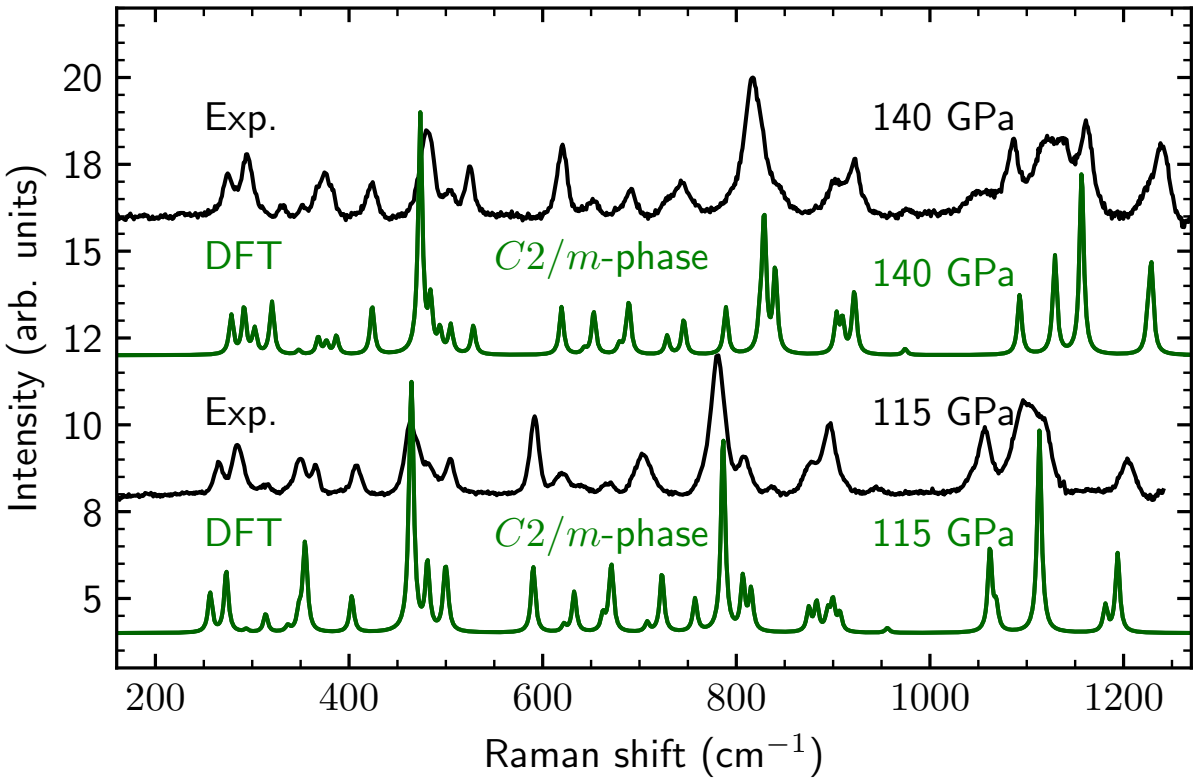

FIG. 5. Comparison between Raman bands of experimental data (black) and theoretical data (green) of $MgCO_3$-II ($C2/m$-phase [38]) at 115 and 140 GPa. Experimental data have been obtained on the temperature quenched sample after heating to ∼3000 and ∼3200 K, respectively. The experimental spectrum reveals the complete transformation of $MgCO_3$ (magnesite) to $MgCO_3$-II at these conditions. DFT frequencies were calculated with a FWHM broadening of 5 cm^{-1}. The calculated frequencies were multiplied by a scaling factor of 1.02. (color online)

ported by Oganov *et al.* [38] and lattice parameters are well in agreement with those from Le Bail refinements for the same pressure range as reported by Maeda *et al.* [9].

Raman spectra of $MgCO_3$ (magnesite) and $MgCO_3$-II ($C2/m$-phase) were measured upon pressure release (Fig. 7 and 2). The pressure unexpectedly dropped during the first step of the release from 85 GPa down to 64 GPa. The pressure was then released in small steps down to ambient conditions, while Raman spectra were measured. During pressure release, the characteristic Raman bands of $MgCO_3$ (magnesite) and those of $MgCO_3$-II ($C2/m$-phase) could concomitantly be observed in the pressure range between 39.6 – 85 GPa. At lower pressures, only the $A_{1g}(\nu_1)$ and $E_g(\nu_4)$ modes of $MgCO_3$ (magnesite) remained. The low frequency E_g modes reappeared at

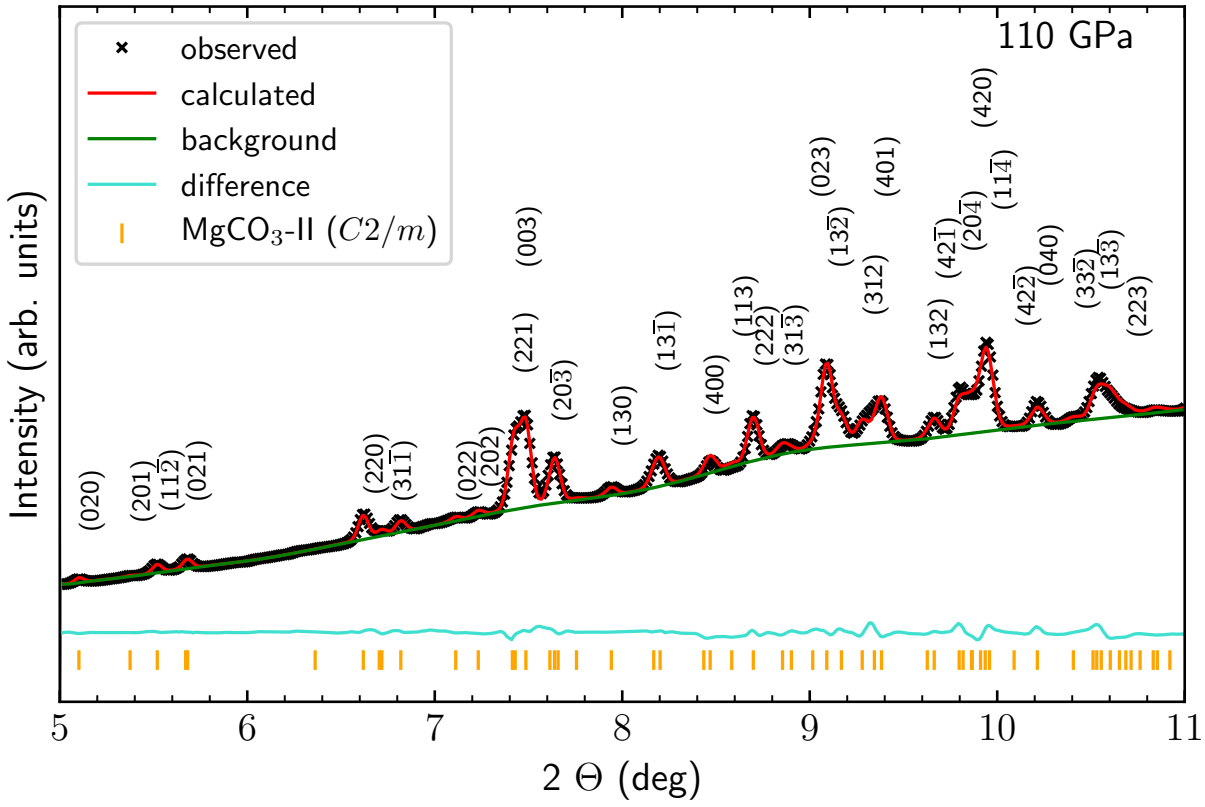

FIG. 6. Rietveld refinement of diffraction data collected at 110 GPa. The structural model by Oganov *et al.* [38] for $MgCO_3$-II ($C2/m$-phase) was used for the refinement (λ = 0.2898 Å). Refined structural parameters are listed in the appendix (Tab. 1-2). (color online)

around 5 GPa. $MgCO_3$ (magnesite) was eventually recovered at ambient conditions, unequivocally showing that no decomposition occured after laser heating at high pressures.

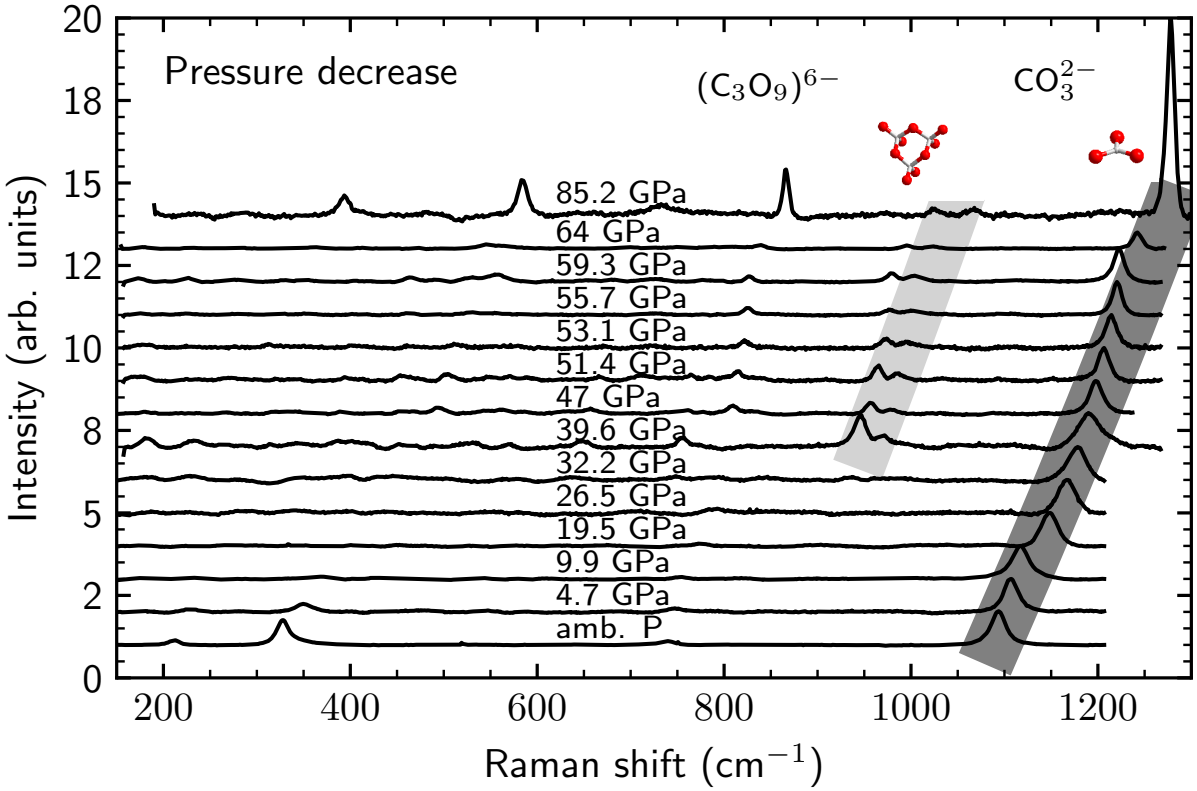

FIG. 7. Raman spectra of $MgCO_3$ (magnesite) + $MgCO_3$-II ($C2/m$) obtained during decompression down to ambient conditions. Frequencies of the $(C_3O_9)^{6-}$ ring bending (light grey) are observed down to ∼40 GPa. The concomitant presence of a characteristic mode (CO_3^{2-}–stretching mode) of $MgCO_3$ (magnesite) indicated in dark grey shows the coexistence of magnesite and metastable $MgCO_3$-II. $MgCO_3$ (magnesite) is recovered at low pressures and ambient conditions. (color online)

C. Phase diagram of $MgCO_3$

Based on the results from this study in conjunction with data from the literature [9, 26, 31, 32, 40, 69] we revise the phase diagram of $MgCO_3$ (Fig. 8). A first phase diagram of $MgCO_3$ was given by Isshiki *et al.* [26] in which phase boundaries were drawn for the magnesite to 'magnesite-II' phase transition and the decomposition behaviour of $MgCO_3$, determined by Fiquet *et al.* [31], was extended to higher P,T-conditions. Another phase diagram at lower P,T-conditions was reported by Solopova *et al.* [32], where the melting- and decomposition behavior of magnesite was described. The slope of the melting curve was discussed to be less steep than that reported by Katsura and Ito [69]. Also, for pressures below 50 GPa the decomposition of $MgCO_3$ (magnesite) was shown to happen at significantly lower temperatures than reported by Fiquet *et al.* [31], while at higher pressures both curves are approaching one another. We combined the contents of the phase diagrams from both studies [26, 32] and added data points obtained in this study (large filled circles in Fig. 8) along with datapoints of the available high pressure high temperature studies on $MgCO_3$ beyond 50 GPa [9, 26, 32, 40]. It should be borne in mind that our data and those by Solopova *et al.* [32] were obtained after temperature quenching and at high pressures, while all other data from the literature were measured in-situ at high pressures and high temperatures [9, 26, 40].

In the present phase diagram, data points of $MgCO_3$ (magnesite) are indicated by black circles (Fig. 8). According to Solopova *et al.* [32] our data points of heated $MgCO_3$ (magnesite) fall within the conditions for magnesite as a solid phase. Our data points of $MgCO_3$-II (yellow circles) and $MgCO_3$-II associated with $MgCO_3$ (black-yellow cirlces) are in very good agreement with the observations by Maeda *et al.* [9] and Boulard *et al.* [40]. Hence, we present the $MgCO_3$–$MgCO_3$-II phase boundary (yellow dashed line) with a negative slope of $\mathrm{d}T/\mathrm{d}P$ = -940 K GPa^{-1} towards higher temperatures. Due to a lack of data, the phase boundary is only drawn up to the maximum available P,T-conditions [40]. Our data points reveal that no decomposition is to be expected for $MgCO_3$-II at P,T-conditions suggested by the decompositon lines of the previous phase diagrams [26, 32] (see appendix Fig. 6). As a consequence, the decomposition boundary of $MgCO_3$-II ($C2/m$-phase) by Isshiki *et al.* [26] is not shown in the revised phase diagram (Fig. 8). Further, $MgCO_3$ (magnesite) is observed to transform into $MgCO_3$-II rather than decomposing into MgO + C + O_2 at pressures and temperatures above 85 GPa and $\sim$3000 K, respectively.

In our experiments, no other phase transition was found for pressures and temperatures up to

148 GPa and $\sim$3600 K. Our conclusion is consistent with the interpretation of Le Bail fits by Boulard *et al.* [40] and Maeda *et al.* [9] who conducted in-situ powder X-ray diffraction in the same P,T-range. These combined observations suggest that the magnesite-II phase, found by Isshiki *et al.* [26], was very likely the $C2/m$-phase ($MgCO_3$-II).

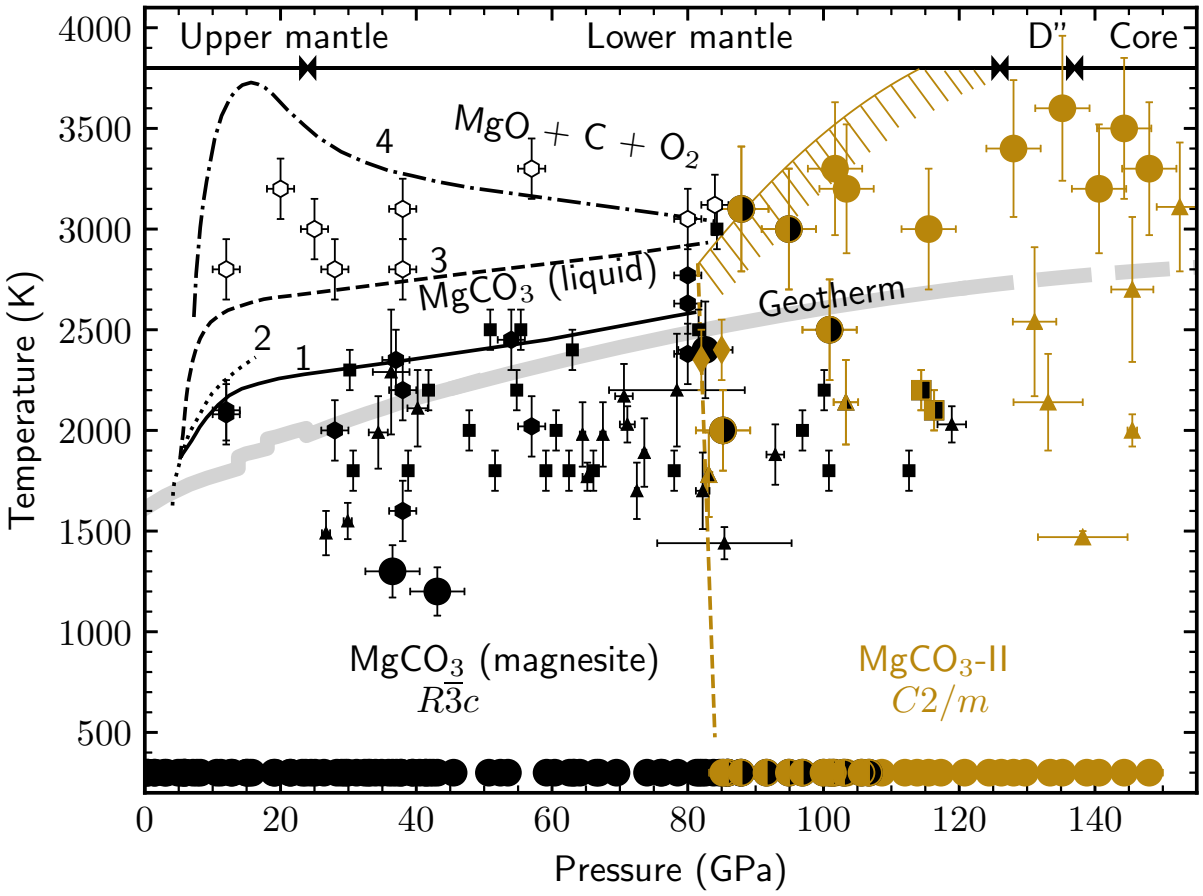

FIG. 8. Phase relations in the $MgCO_3$ system with respect to the depth profile of the Earth's mantle and outtermost core. Markers correspond to studies, while colours denote distinct phases (black = magnesite, yellow = $C2/m$-phase [38], white = magnesite + MgO). Data from this study are shown as large circles and were obtained after temperature quenching at high pressures. Data obtained by Solopova *et al.* [32] are shown as hexagons, which have also been obtained after temperature quenching at high pressures. Squares, triangles, and diamonds correspond to the in situ data obtained in the studies by Isshiki *et al.* [26], Maeda *et al.* [9], and Boulard *et al.* [40], respectively. A typical mantle geotherm is shown as grey solid line [70]. The solid (1) and dashed (3) lines represent liquidus and decomposition for magnesite as reported by Solopova *et al.* [32]. The dotted line (2) represents the liquidus for magnesite as reported by Katsura and Ito [69]. The dash-dotted line (4) represents the decomposition of $MgCO_3$ as reported by Fiquet *et al.* [31]. The dashed yellow line corresponds to the phase boundary of magnesite into the $C2/m$-phase derived here. The broad dashed yellow band presents a boundary above which we have not observed decomposition, but solid or liquid $MgCO_3$-II. (color online)

IV. CONCLUSIONS

This study provides the first Raman spectra of pure $MgCO_3$ at pressures and temperatures up to 148 GPa and 3600 K. Our spectra allowed the identification of $MgCO_3$-II-tetracarbonate and the location of the phase boundary between $MgCO_3$ (magnesite) and $MgCO_3$-II ($C2/m$-phase). Based on our observations from Raman spectroscopy, XRD and density functional theory calculations, we propose a revised phase diagram for $MgCO_3$. At P, T-conditions of Earth's upper mantle and upper part of the lower mantle (e.g. pressures up to $\sim$80 GPa and temperatures up to $\sim$2500 K), $MgCO_3$ is stable as magnesite ($R\bar{3}c$) [26, 32]. At P, T-conditions of Earth's lowermost mantle and outermost core (e.g. 85-148 GPa and at temperatures above 2500 K) the stable polymorph $MgCO_3$-II is a monoclinic $C2/m$-tetracarbonate as predicted by Oganov *et al.* [38]. In the present study we observe that $MgCO_3$-II can exist on pressure release down to $\sim$40 GPa. This is similar to an earlier observation of the existance of $CaCO_3$-tetracarbonate on pressure release down to 57 GPa [45].

V. ACKNOWLEDGEMENTS

The authors acknowledge funding by the Deutsche Forschungsgemeinschaft (DFG)-Germany (FOR2125/CarboPaT, BA4020, WI1232) and BMBF (05K16RFA). Chris J. Pickard is supported by the Royal Society through a Royal Society Wolfson Research Merit Award and the EPSRC through Grant No. EP/P022596/1. Sergey S. Lobanov acknowledges the support of the Helmholtz Young Investigators Group CLEAR (VH-NG-1325). The '$2n+1$' Raman theorem in CASTEP was developed under grant EP/I030107/1. DESY (Hamburg, Germany), a member of the Helmholtz Association (HGF) is acknowledged for the provision of experimental facilities. We would like to thank Hanns-Peter Liermann and his team for assistance in using beamline P02.2.

See Supplemental Material at [URL will be inserted by publisher].

[1] R. Dasgupta and M. M. Hirschmann, The deep carbon cycle and melting in Earth's interior, Earth and Planetary Science Letters **298**, 1 (2010).

[2] P. B. Kelemen and C. E. Manning, Reevaluating carbon fluxes in subduction zones, what goes down, mostly comes up, Proceedings of the National Academy of Sciences **112**, E3997 (2015).

[3] T. Plank and C. H. Langmuir, The chemical composition of subducting sediment and its consequences for the crust and mantle, Chemical geology **145**, 325 (1998).

[4] N. H. Sleep and K. Zahnle, Carbon dioxide cycling and implications for climate on ancient Earth, Journal of Geophysical Research: Planets **106**, 1373 (2001).

[5] P. Clift and P. Vannucchi, Controls on tectonic accretion versus erosion in subduction zones: Implications for the origin and recycling of the continental crust, Reviews of Geophysics **42**, (2004).

[6] P. D. Clift, A revised budget for Cenozoic sedimentary carbon subduction, Reviews of Geophysics **55**, 97 (2017).

[7] V. Stagno, Y. Tange, N. Miyajima, C. McCammon, T. Irifune, and D. Frost, The stability of magnesite in the transition zone and the lower mantle as function of oxygen fugacity, Geophysical Research Letters **38**, (2011).

[8] Y. N. Palyanov, Y. V. Bataleva, A. G. Sokol, Y. M. Borzdov, I. N. Kupriyanov, V. N. Reutsky, and N. V. Sobolev, Mantle–slab interaction and redox mechanism of diamond formation, Proceedings of the National Academy of Sciences **110**, 20408 (2013).

[9] F. Maeda, E. Ohtani, S. Kamada, T. Sakamaki, N. Hirao, and Y. Ohishi, Diamond formation in the deep lower mantle: A high-pressure reaction of $MgCO_3$ and SiO_2, Scientific reports **7**, 40602 (2017).

[10] S. M. Dorfman, J. Badro, F. Nabiei, V. B. Prakapenka, M. Cantoni, and P. Gillet, Carbonate stability in the reduced lower mantle, Earth and Planetary Science Letters **489**, 84 (2018).

[11] H. Keppler, M. Wiedenbeck, and S. S. Shcheka, Carbon solubility in olivine and the mode of carbon storage in the Earth's mantle, Nature **424**, 414 (2003).

[12] S. S. Shcheka, M. Wiedenbeck, D. J. Frost, and H. Keppler, Carbon solubility in mantle minerals, Earth and Planetary Science Letters **245**, 730 (2006).

[13] M. Walter, G. Bulanova, L. Armstrong, S. Keshav, J. Blundy, G. Gudfinnsson, O. Lord, A. Lennie, S. Clark, C. Smith, *et al.*, Primary carbonatite melt from deeply subducted oceanic crust, Nature **454**,

622 (2008).

[14] K. F. Dziubek, M. Ende, D. Scelta, R. Bini, M. Mezouar, G. Garbarino, and R. Miletich, Crystalline polymeric carbon dioxide stable at megabar pressures, Nature communications **9**, 3148 (2018).

[15] D. J. Frost and C. A. McCammon, The redox state of Earth's mantle, Annual Review of Earth and Planetary Sciences **36**, 389 (2008).

[16] R. Dasgupta, A. Buono, G. Whelan, and D. Walker, High-pressure melting relations in Fe–C–S systems: Implications for formation, evolution, and structure of metallic cores in planetary bodies, Geochimica et Cosmochimica Acta **73**, 6678 (2009).

[17] M. J. Walter, S. C. Kohn, D. Araujo, G. P. Bulanova, C. B. Smith, E. Gaillou, J. Wang, A. Steele, and S. B. Shirey, Deep mantle cycling of oceanic crust: Evidence from diamonds and their mineral inclusions, Science **334**, 54 (2011).

[18] N. Martirosyan, T. Yoshino, A. Shatskiy, A. Chanyshev, and K. Litasov, The $CaCO_3$–Fe interaction: Kinetic approach for carbonate subduction to the deep Earth's mantle, Physics of the Earth and Planetary Interiors **259**, 1 (2016).

[19] S. Goes, R. Agrusta, J. Van Hunen, and F. Garel, Subduction-transition zone interaction: A review, Geosphere **13**, 644 (2017).

[20] T. R. McGetchin and J. Besancon, Carbonate inclusions in mantle-derived pyropes, Earth and Planetary Science Letters **18**, 408 (1973).

[21] A. Wang, J. D. Pasteris, H. O. Meyer, and M. L. Dele-Duboi, Magnesite-bearing inclusion assemblage in natural diamond, Earth and Planetary Science Letters **141**, 293 (1996).

[22] C.-T. Lee, R. L. Rudnick, W. F. McDonough, and I. Horn, Petrologic and geochemical investigation of carbonates in peridotite xenoliths from northeastern Tanzania, Contributions to Mineralogy and Petrology **139**, 470 (2000).

[23] F. E. Brenker, C. Vollmer, L. Vincze, B. Vekemans, A. Szymanski, K. Janssens, I. Szaloki, L. Nasdala, W. Joswig, and F. Kaminsky, Carbonates from the lower part of transition zone or even the lower mantle, Earth and Planetary Science Letters **260**, 1 (2007).

[24] F. Kaminsky, Mineralogy of the lower mantle: A review of 'super-deep' mineral inclusions in diamond, Earth-Science Reviews **110**, 127 (2012).

[25] F. V. Kaminsky, I. D. Ryabchikov, and R. Wirth, A primary natrocarbonatitic association in the Deep Earth, Mineralogy and Petrology **110**, 387 (2016).

[26] M. Isshiki, T. Irifune, K. Hirose, S. Ono, Y. Ohishi, T. Watanuki, E. Nishibori, M. Takata, and

M. Sakata, Stability of magnesite and its high-pressure form in the lowermost mantle, Nature **427**, 60 (2004).

[27] A. Rohrbach and M. W. Schmidt, Redox freezing and melting in the earth's deep mantle resulting from carbon–iron redox coupling, Nature **472**, 209 (2011).

[28] L. Bayarjargal, C.-J. Fruhner, N. Schrodt, and B. Winkler, $CaCO_3$ phase diagram studied with raman spectroscopy at pressures up to 50 GPa and high temperatures and DFT modeling, Physics of the Earth and Planetary Interiors **281**, 31 (2018).

[29] J. Binck, S. Chariton, M. Stekiel, L. Bayarjargal, W. Morgenroth, V. Milman, L. Dubrovinsky, and B. Winkler, High-pressure, high-temperature phase stability of iron-poor dolomite and the structures of dolomite-IIIc and dolomite-V, Physics of the Earth and Planetary Interiors **299**, 106403 (2020).

[30] V. Cerantola, E. Bykova, I. Kupenko, M. Merlini, L. Ismailova, C. McCammon, M. Bykov, A. I. Chumakov, S. Petitgirard, I. Kantor, V. Svitlyk, J. Jacobs, M. Hanfland, M. Mezouar, C. Prescher, R. Rüffer, V. B. Prakapenka, and L. Dubrovinsky, Stability of iron-bearing carbonates in the deep Earth's interior, Nature Communications **8**, 15960 (2017).

[31] G. Fiquet, F. Guyot, M. Kunz, J. Matas, D. Andrault, and M. Hanfland, Structural refinements of magnesite at very high pressure, American Mineralogist **87**, 1261 (2002).

[32] N. Solopova, L. Dubrovinsky, A. Spivak, Y. A. Litvin, and N. Dubrovinskaia, Melting and decomposition of $MgCO_3$ at pressures up to 84 GPa, Physics and Chemistry of Minerals **42**, 73 (2015).

[33] X. Yao, C. Xie, X. Dong, A. R. Oganov, and Q. Zeng, Novel high-pressure calcium carbonates, Physical Review B **98**, 014108 (2018).

[34] S. S. Santos, M. L. Marcondes, J. F. Justo, and L. V. Assali, Stability of calcium and magnesium carbonates at Earth's lower mantle thermodynamic conditions, Earth and Planetary Science Letters **506**, 1 (2019).

[35] N. V. Skorodumova, A. B. Belonoshko, L. Huang, R. Ahuja, and B. Johansson, Stability of the $MgCO_3$ structures under lower mantle conditions, American mineralogist **90**, 1008 (2005).

[36] S. Arapan, J. Souza de Almeida, and R. Ahuja, Formation of sp^3 Hybridized Bonds and Stability of $CaCO_3$ at Very High Pressure, Physical Review Letters **98**, 268501 (2007).

[37] A. R. Oganov, C. W. Glass, and S. Ono, High-pressure phases of $CaCO_3$: *C*rystal structure prediction and experiment, Earth and Planetary Science Letters **241**, 95 (2006).

[38] A. R. Oganov, S. Ono, Y. Ma, C. W. Glass, and A. Garcia, Novel high-pressure structures of $MgCO_3$, $CaCO_3$ and CO_2 and their role in Earth's lower mantle, Earth and Planetary Science Letters **273**, 38

(2008).

[39] C. J. Pickard and R. J. Needs, Structures and stability of calcium and magnesium carbonates at mantle pressures, Physical Review B **91**, 104101 (2015).

[40] E. Boulard, A. Gloter, A. Corgne, D. Antonangeli, A.-L. Auzende, J.-P. Perrillat, F. Guyot, and G. Fiquet, New host for carbon in the deep Earth, Proceedings of the National Academy of Sciences **108**, 5184 (2011).

[41] E. Boulard, N. Menguy, A. L. Auzende, K. Benzerara, H. Bureau, D. Antonangeli, A. Corgne, G. Morard, J. Siebert, J. P. Perrillat, F. Guyot, and G. Fiquet, Experimental investigation of the stability of Fe-rich carbonates in the lower mantle, Journal of Geophysical Research: Solid Earth **117**, (2012).

[42] E. Boulard, D. Pan, G. Galli, Z. Liu, and W. L. Mao, Tetrahedrally coordinated carbonates in Earth's lower mantle, Nature communications **6**, 6311 (2015).

[43] M. Merlini, M. Hanfland, A. Salamat, S. Petitgirard, and H. Müller, The crystal structures of $Mg_2Fe_2C_4O_{13}$, with tetrahedrally coordinated carbon, and $Fe_{13}O_{19}$, synthesized at deep mantle conditions, American Mineralogist **100**, 2001 (2015).

[44] M. Merlini, V. Cerantola, G. D. Gatta, M. Gemmi, M. Hanfland, I. Kupenko, P. Lotti, H. Müller, and L. Zhang, Dolomite-IV: Candidate structure for a carbonate in the Earth's lower mantle, American Mineralogist **102**, 1763 (2017).

[45] S. S. Lobanov, X. Dong, N. S. Martirosyan, A. I. Samtsevich, V. Stevanovic, P. N. Gavryushkin, K. D. Litasov, E. Greenberg, V. B. Prakapenka, A. R. Oganov, *et al.*, Raman spectroscopy and x-ray diffraction of sp^3 $CaCO_3$ at lower mantle pressures, Physical Review B **96**, 104101 (2017).

[46] S. Chariton, M. Bykov, E. Bykova, E. Koemets, T. Fedotenko, B. Winkler, M. Hanfland, V. B. Prakapenka, E. Greenberg, C. McCammon, and L. Dubrovinsky, The crystal structure of the Fe-bearing $MgCO_3$ sp^3-carbonate at 98 GPa from single-crystal X-ray diffraction (2019), unpublished.

[47] A. Spivak, N. Solopova, V. Cerantola, E. Bykova, E. Zakharchenko, L. Dubrovinsky, and Y. Litvin, Raman study of $MgCO_3$–$FeCO_3$ carbonate solid solution at high pressures up to 55 GPa, Physics and Chemistry of Minerals **41**, 633 (2014).

[48] I. Efthimiopoulos, S. Jahn, A. Kuras, U. Schade, and M. Koch-Müller, Combined high-pressure and high-temperature vibrational studies of dolomite: Phase diagram and evidence of a new distorted modification, Physics and Chemistry of Minerals **44**, 465 (2017).

[49] C. E. Vennari and Q. Williams, A novel carbon bonding environment in deep mantle high-pressure dolomite, American Mineralogist **103**, 171 (2018).

[50] Q. Williams, B. Collerson, and E. Knittle, Vibrational spectra of magnesite ($MgCO_3$) and calcite-III at high pressures, American Mineralogist **77**, 1158 (1992).

[51] P. Gillet, Stability of magnesite ($MgCO_3$) at mantle pressure and temperature conditions: A Raman spectroscopic study, American Mineralogist **78**, 1328 (1993).

[52] S. Ni, T. Li, and X. Yang, Hydrothermal synthesis of $MgCO_3$ and its optical properties, Journal of Alloys and Compounds **509**, 7874 (2011).

[53] B. H. Toby and R. B. Von Dreele, *GSAS-II*: the genesis of a modern open-source all purpose crystallography software package, Journal of Applied Crystallography **46**, 544 (2013).

[54] S. Göttlicher and A. Vegas, Electron-density distribution in magnesite ($MgCO_3$), Acta Crystallographica Section B: Structural Science **44**, 362 (1988).

[55] R. Boehler, New diamond cell for single-crystal X-ray diffraction, Review of Scientific Instruments **77**, 115103 (2006).

[56] H. Mao, P. Bell, J. t. Shaner, and D. Steinberg, Specific volume measurements of Cu, Mo, Pd, and Ag and calibration of the ruby R1 fluorescence pressure gauge from 0.06 to 1 Mbar, Journal of applied physics **49**, 3276 (1978).

[57] H. Mao, J.-A. Xu, and P. Bell, Calibration of the ruby pressure gauge to 800 kbar under quasi-hydrostatic conditions, Journal of Geophysical Research: Solid Earth **91**, 4673 (1986).

[58] Y. Akahama and H. Kawamura, Pressure calibration of diamond anvil Raman gauge to 310 GPa, Journal of Applied Physics **100**, 043516 (2006).

[59] A. Dewaele, P. Loubeyre, and M. Mezouar, Equations of state of six metals above 94 GPa, Physical Review B **70**, 094112 (2004).

[60] L. R. Benedetti and P. Loubeyre, Temperature gradients, wavelength-dependent emissivity, and accuracy of high and very-high temperatures measured in the laser-heated diamond cell, High Pressure Research **24**, 423 (2004).

[61] C. Prescher and V. B. Prakapenka, DIOPTAS: a program for reduction of two-dimensional X-ray diffraction data and data exploration, High Pressure Research **35**, 223 (2015), https://doi.org/10.1080/08957959.2015.1059835.

[62] S. J. Clark, M. D. Segall, C. J. Pickard, P. J. Hasnip, M. I. Probert, K. Refson, and M. C. Payne, First principles methods using CASTEP, Zeitschrift für Kristallographie-Crystalline Materials **220**, 567 (2005).

[63] K. Lejaeghere, G. Bihlmayer, T. Björkman, P. Blaha, S. Blügel, V. Blum, D. Caliste, I. E. Castelli,

S. J. Clark, A. Dal Corso, and et al., Reproducibility in density functional theory calculations of solids, Science **351**, (2016).

[64] J. P. Perdew, K. Burke, and M. Ernzerhof, Generalized gradient approximation made simple, Physical review letters **77**, 3865 (1996).

[65] H. J. Monkhorst and J. D. Pack, Special points for Brillouin-zone integrations, Physical review B **13**, 5188 (1976).

[66] K. Miwa, Prediction of raman spectra with ultrasoft pseudopotentials, Physical Review B **84**, 094304 (2011).

[67] H. Rutt and J. Nicola, Raman spectra of carbonates of calcite structure, Journal of Physics C: Solid State Physics **7**, 4522 (1974).

[68] W. D. Bischoff, S. K. Sharma, and F. T. MacKenzie, Carbonate ion disorder in synthetic and biogenic magnesian calcites: A Raman spectral study, American Mineralogist **70**, 581 (1985).

[69] T. Katsura and E. Ito, Melting and subsolidus phase relations in the $MgSiO_3$–$MgCO_3$ system at high pressures: implications to evolution of the Earth's atmosphere, Earth and Planetary Science Letters **99**, 110 (1990).

[70] T. Katsura, A. Yoneda, D. Yamazaki, T. Yoshino, and E. Ito, Adiabatic temperature profile in the mantle, Physics of the Earth and Planetary Interiors **183**, 212 (2010).